Inflatable origami: multimodal deformation via multistability

David Melancon[a,*], **Antonio Elia Forte**[a,b,c,*], **Leon M. Kamp**[a,d], **Benjamin Gorissen**[a], **and Katia Bertoldi**[a,†]

[a]J.A. Paulson School of Engineering and Applied Sciences, Harvard University, Cambridge, MA 02138, USA; [b]Department of Electronics, Information and Bioengineering, Politecnico di Milano, Milan, 20133 Italy; [c]Department of Engineering, King's College London, London, WC2R 2LS, UK; [d]Department of Applied Physics, Eindhoven University of Technology, Postbus 513, 5600 MB, Eindhoven, The Netherlands; [*]These authors contributed equally to this work; [†]Corresponding author. Email: bertoldi@seas.harvard.edu

Inflatable structures have become essential components in the design of soft robots and deployable systems as they enable dramatic shape change from a single pressure inlet. This simplicity, however, often brings a strict limitation: unimodal deformation upon inflation. Here, we embrace multistability to design modular, inflatable structures that can switch between distinct deformation modes as a response to a single input signal. Our system comprises bistable origami modules in which pressure is used to trigger a snap-through transition between a state of deformation characterized by simple deployment to a state characterized by bending deformation. By assembling different modules and tuning their geometry to cause snapping at different pressure thresholds, we create structures capable of complex deformations that can be pre-programmed and activated using only one pressure source. Our approach puts forward multistability as a paradigm to eliminate a one-to-one relation between input signal and deformation mode in inflatable systems.

Origami | Multistability | Inflatables

Introduction

When safe human-machine interaction is paramount, the design of smart devices and robotic systems often relies on inflatables and cylindrical structures as they support a variety of possible deformations (1–7). However, the vast majority of these suffer from an intrinsic one-to-one relationship between input pressure and output deformation. In other words, they exhibit increasing unimodal deformation with pressure (8–10). To compensate for this deficiency, common strategies include sequencing multiple elements (11–17) or pressurizing chambers independently (18, 19). Alternatively, material inextensibility (20) and non-linearities (21, 22) have been harnessed to achieve bidirectional bending. Despite all this, targeting arbitrary deformation modes with a single pressure input is beyond the capabilities of current inflatable systems.

In the wider domain of adaptive systems, origami principles have extensively been employed to realize transformable architectures (23–28), self-foldable machines (29–31), and waveguides (32–35). Distributed actuation approaches have been used to directly control the fold angle via pressurized air pockets (36) or stimuli-responsive materials (24, 37–40). However, these strategies require multiple input sources and result in bulky assemblies with excessive tethering and/or slow actuation. To overcome these limitations, recent efforts have achieved shape control of origami structures with embedded ferromagnetic elements via remote magnetic fields (41–43).

Additionally, if the origami crease pattern supports a non-convex energy landscape, multiple stable states manifest (42, 44–51), which can expand the functionality of the structures. For example, introducing multistability in the classic waterbomb origami pattern resulted in the creation of mechanical bits and logic elements (45, 52, 53); multistable origami sheets based on the tiling of the degree-four vertex enabled the design of self-locking grippers (54) and energy-absorbing components for drones (55); finally, bistable configurations of the Kresling pattern (46, 56) have been exploited to (i) generate locomotion via peristaltic motion (57) or differential friction (58), (ii) create flexible joints for robotic manipulation (59), and (iii) store mechanical memory (42, 60).

Here, we employ the Kresling pattern as a building block to realize inflatable cylindrical structures capable of supporting multiple deformation modes, while being globally actuated using a single pressure input. We start with a monostable Kresling pattern and modify it by introducing two additional valley creases in one of its panels (see Fig. 1). This makes the panel bistable, so that during inflation it unfolds and snaps outward, breaking the rotational symmetry of the module. Importantly, upon vacuum such asymmetry gives rise to bending, which persists until a critical negative pressure is reached at which the panel snaps back. Next, we show that these modules can be geometrically programmed to snap at different pressure thresholds and assembled in various order and orientation to form structures capable of multimodal deformation. Distinct deformation modes can be first activated by snapping a selected set of modules and then triggered by applying vacuum. Such modes can be inverse-designed by optimizing the arrangement and orientation of the building blocks. Importantly, the same structure can shape-shift to multiple target deformation modes using only one pressure input. Our approach paves the way for new opportunities in the design of reconfigurable structures with embedded actuation.

Our building blocks based on the Kresling pattern

To realize multimodal origami structures, we use building blocks that consist of one layer of the classic Kresling pattern (also known as nejiri ori) (56). More specifically, in its initial, undeformed state, the single module is capped by two hexagonal facets with edges of length $l = 30$ mm, separated by a distance $h = 24$ mm, and rotated by an angle $\alpha = 30^\circ$ with respect to each other (see Fig. 1a). The hexagons are connected at each side by a panel comprising a pair of triangular facets coupled by alternating mountain (i.e. edges $A'B$ and AB') and valley (i.e. edge BB') folds. Since the Kresling pattern is not rigid foldable (46), any change in its internal volume will lead to an incompatible configuration. To accommodate the resulting geometrical frustration, we 3D-print 1-mm thick triangular facets out of a compliant material (TPU95A from

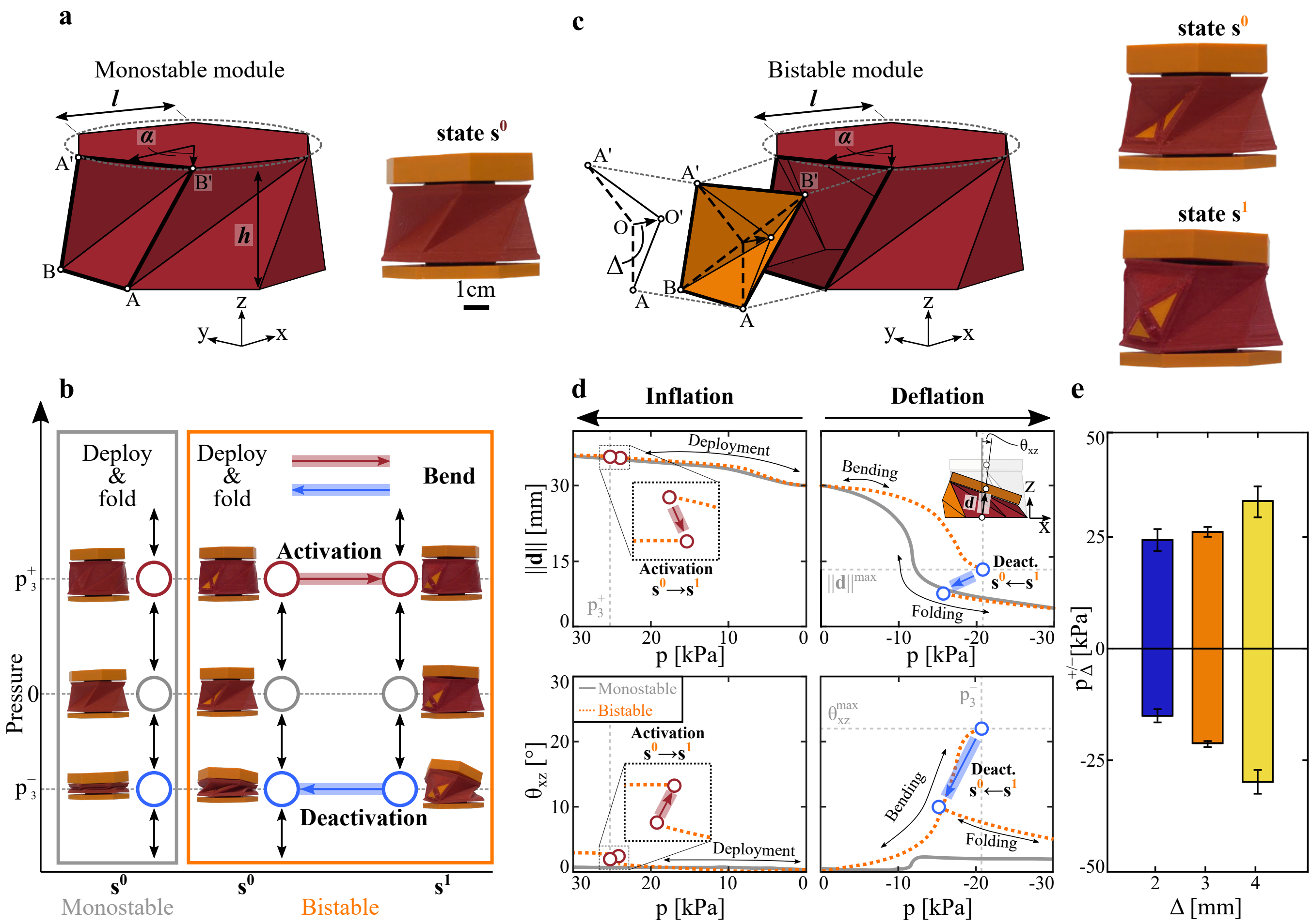

Fig. 1. Bistable origami modules as building blocks for multi-output, single-input inflatable structures. **(a)** Schematics of a monostable module based on the hexagonal-base Kresling origami pattern, along with a 3D-printed prototype. The panels of the monostable modules remain always folded inward. We refer to this state of deformation as state s^0. **(b)** State diagram of the pressurized origami modules. **(c)** Bistable module with a modified panel (highlighted in orange) made of four triangular facets $A'BO'$, $AO'B'$, $AO'B$, and $A'B'O'$ and characterized by a depth Δ from vertex O to O', along with a 3D-printed prototype displayed in its two stable states: state s^0 for which all panels (including the modified panel) are folded inward; and state s^1 for which the modified panel is popped outward (while all other panels are still folded inward). **(d)** Norm of the vector connecting the two caps' centroids, $||\mathbf{d}||$, and bending angle, θ_{xz}, vs. pressure, p, for the monostable (solid gray curves) and bistable with $\Delta = 3$ mm (dashed orange curves) origami modules during inflation and deflation. **(e)** Experimental positive and negative pressure thresholds, p_Δ^+ and p_Δ^-, as a function of the modified panel's depth, Δ.

Ultimaker with Young's modulus $E = 26$ MPa) and reduce the thickness locally to 0.4 mm to create the hinges (see prototype in Fig. 1a). Further, to facilitate coupling between different modules, we 3D-print the hexagonal caps out of a stiffer material (PLA from Ultimaker with Young's modulus $E = 2.3$ GPa). Additionally, we coat the origami unit with a thin layer of polydimethylsiloxane (PDMS) to form an inflatable cavity (see Supplementary Materials, Section S1 for fabrication details). Note that the chosen values of the parameters (h, l, α) yield a monostable origami module (i.e. the Kresling pattern is only stable in its initial, undeformed state).

To investigate the response of a single module, we position it on a flat surface and slowly inflate it with air at a rate of 10 mL/min using a syringe pump (Pump 33DS, Harvard Apparatus). We monitor the pressure using a sensor (Honeywell ASDXRRX015PDAA5) and capture the module's deformation via two digital cameras (SONY RX100 V) positioned in front and above it (see Supplementary Materials, Section S2 for details). As expected (46), the Kresling unit deploys and folds upon inflation and deflation and returns to its undeformed configuration as soon as the pressure is removed (Fig. 1b). This state of deformation, in which all panels are folded inward, is referred to as s^0. To better characterize the response of the module, we monitor the position of its top cap and record the vector connecting the two caps' centroids, $\mathbf{d}$. In Fig. 1d, we report the norm of $\mathbf{d}$, $||\mathbf{d}||$, and the angle between the projection of $\mathbf{d}$ on the xz-plane and the positive z-axis, θ_{xz}, as a function of the internal pressure, p. We find that $||\mathbf{d}||$ increases from 30 mm to 36 mm during inflation and then decreases to 4 mm during deflation. Differently, θ_{xz} remains close to zero during the entire test (see gray curves in Fig. 1d), indicating that the module purely deploys upon inflation and folds upon deflation, deforming exclusively along its central axis.

Aiming at unlocking different deformation modes with one single pressure input, we then take inspiration from bistability in degree-four vertices (48, 53, 61) and modify one of the original Kresling panels by introducing two additional valley creases (i.e. AO and $A'O$ with O being the midpoint of crease BB', see Fig. 1c). While this effectively creates a degree-four vertex, it results in a monostable origami unit, as no snap-through instability is recorded upon inflation (see Supplementary Materials, Section S2 for details). To increase the geometric incompatibility during deployment and achieve bistability in the unit, we then move the degree-four vertex inward by Δ (see Fig. 1c where Δ is the norm of vector $\overline{OO'}$ perpendicular to vectors $\overline{AA'}$ and $\overline{BB'}$).

Choosing $\Delta = 3$ mm, for example, we can fabricate an origami unit that can easily transition between two stable states: state s^0 for which all panels are folded inward, and state s^1 for which the modified panel is popped outward (while all other panels are still folded inward - Fig. 1c). Similar to the unit based on the classic Kresling pattern, upon inflation this modified module deploys with all panels bent inward if $p < 26.1 \pm 0.9$ kPa. However, at $p_3^+ = 26.1 \pm 0.9$ kPa (where the subscript refers to $\Delta = 3$ mm and the superscript refers to positive pressure), the unit snaps from state s^0 to state s^1, which is characterized by the modified panel popped outward (Fig. 1b)—a transition that results in a sudden small drop of $||\mathbf{d}||$ and slight increase of θ_{xz} (see zoom-in in Fig. 1d, left hand side). Finally, a further increase in pressure causes the unit to elongate until the maximum structural limit is reached. Afterward, when the input pressure is removed, the modified panel remains popped outward because of bistability. As such, when we apply negative pressure, the unit not only folds, but also bends (see Fig. 1b), exhibiting a behaviour that radically differs from that of the monostable Kresling module. In fact, we find that the vector $\mathbf{d}$ decreases in length and rotates in space. To characterize such rotation, we position the module with the modified panel facing the negative x-direction and monitor the angle θ_{xz}. We find that θ_{xz} monotonically increases until the two hexagonal caps come into physical contact, effectively clipping the available range of bending deformation to $\theta_{xz}^{max} = 21.7 \pm 0.3\,^\circ$ (see Fig. 1d). As previously mentioned, this bending deformation is activated by the snapping of the modified panel, which remains in the popped outward configuration (while the other panels fold under increasing negative pressure) and breaks the radial symmetry. Note that, as the Kresling twists when deflating, $\mathbf{d}$ also rotates in the xy-plane. Specifically, at p_3^- the angle between the projection of $\mathbf{d}$ on the xy-plane and the positive x-axis is $\theta_{xy} = 10.6 \pm 0.6\,^\circ$ (see Supplementary Materials, Section S2 for details). Finally, when the negative pressure passes the threshold $p_3^- = -21.2 \pm 0.7$ kPa (where the superscript refers to negative pressure), the modified panel snaps back to the inward position (see Fig. 1b). At this point θ_{xz} suddenly decreases (see Fig. 1d) and the bending deformation mode gets deactivated. If one continues to apply negative pressure to the module, the unit folds (almost) flat with $||\mathbf{d}|| = 3.8 \pm 0.8$ mm, $\theta_{xz} = 6.9 \pm 0.9^\circ$ and $\theta_{xy} = 22 \pm 0.5^\circ$ at $p = -30$ kPa (see Fig. 1d and Supplementary Materials, Section S2).

Next, we investigate the effect of the depth Δ of our degree-four vertex panel on the positive and negative pressure thresholds, p_Δ^+ and p_Δ^-, as well as the deformed configurations reached upon snapping. The experimental results reported in Fig. 1e for $\Delta = 2$, 3, and 4 mm indicate that the absolute value of the pressure thresholds increases with Δ within the considered range. By contrast, when the units are in state s^1, we find that for all considered Δ, the angles reach $\theta_{xz}^{max} \approx 20^\circ$ and $\theta_{xy}^{max} \approx 10^\circ$ upon vacuum—a value determined by the contact between the caps and the geometry of the Kresling pattern, respectively (see Supplementary Materials, Section S2 for details). Finally, we note that for $\Delta < 2$ mm the modules are found to be monostable. This means that negligible bending is recorded upon application of negative pressure, since the degree-four vertex panel snaps back immediately. Differently, for $\Delta \geq 4$ mm, the positive pressure required to snap the modified panel outward is so high that the module fails (see Fig. S4).

Multimodal deformation via multistability

After demonstrating that our bistable module can transition between two stable states (i.e. states s^0 and s^1) with distinct deformation modes (i.e. deployment/folding and bending), we next combine these units to form multimodal tubular structures whose deformation is controlled by a single pressure input. By connecting n modules, we can construct $(3 \times 2 \times 6 + 1 \times 2)^n = 38^n$ different structures. This is because for each module k we can select (i) either a regular Kresling pattern or a unit comprising a modified, degree-four vertex panel with depth $\Delta^k \in \{2, 3, 4\}$ mm (Fig. 2a); (ii) the chirality of the origami pattern (i.e. the rotation direction of the upper cap with respect to the bottom one), $c^k \in \{//, \backslash\backslash\}$ (Fig. 2b), and (iii) the side on which the modified panel is located, $f^k \in \{1, \ldots, 6\}$ (note that for the modified panel of the bottom unit we choose $f^1 = 1$, since it always faces the negative x-axis—Fig. 2c).

For simplicity, we start by considering structures with $\Delta \in \{2, 4\}$ mm. In Fig. 2d, we show the state diagram of such structures. This is characterized by four pressure thresholds. The positive pressure thresholds p_2^+ and p_4^+ corresponds to the pressures at which the modified panels of all units with $\Delta = 2$ mm and $\Delta = 4$ snap outward, respectively. Equally, the negative thresholds p_2^- and p_4^- correspond to the pressures at which the panels snap inward. These thresholds lead to four distinct stable states, s^{ij} with $i, j \in \{0, 1\}$, where the subscripts i and j refer to the state of the modified panels with $\Delta = 2$ and 4 mm, respectively. The state diagram also establishes the pressure history one has to apply in order to reach each stable state. It shows that the stable states s^{10} and s^{11} can be readily obtained by simply increasing pressure, whereas a more complex pressure path is required to achieve state s^{01}, as one has to (i) increase pressure above p_4^+ and then (ii) decrease it below p_2^-.

While the state diagram in Fig. 2d applies to all tubular structures assembled using modules with $\Delta = 2$ and 4 mm, the deformation modes associated to each stable state upon vacuum depend on the arrangement of the modules. To illustrate this, we consider two structures comprising one module with $\Delta = 2$ mm and another one with $\Delta = 4$ mm connected via 3D-printed screws (see Fig. S2 for details). In the first structure, the two modules have opposite chirality and the modified panels facing the negative x-axis (i.e. $[\Delta^1 c^1 f^1;\, \Delta^2 c^2 f^2] = [2\backslash\backslash 1; 4//1]$ - note that we assume the first unit to be the one at the bottom), whereas in the second one the two modules have the same chirality and modified panels located on the opposite sides of the structure (i.e. $[\Delta^1 c^1 f^1;\, \Delta^2 c^2 f^2] = [2\backslash\backslash 1; 4\backslash\backslash 4]$). The experimental snapshots reported in Figs. 2e and 2f (on the right hand side) show that under vacuum both structures simply fold in state s^{00}, but support more complex deformations in states s^{10}, s^{11}, and s^{01}. To better characterize these complex deformations, we

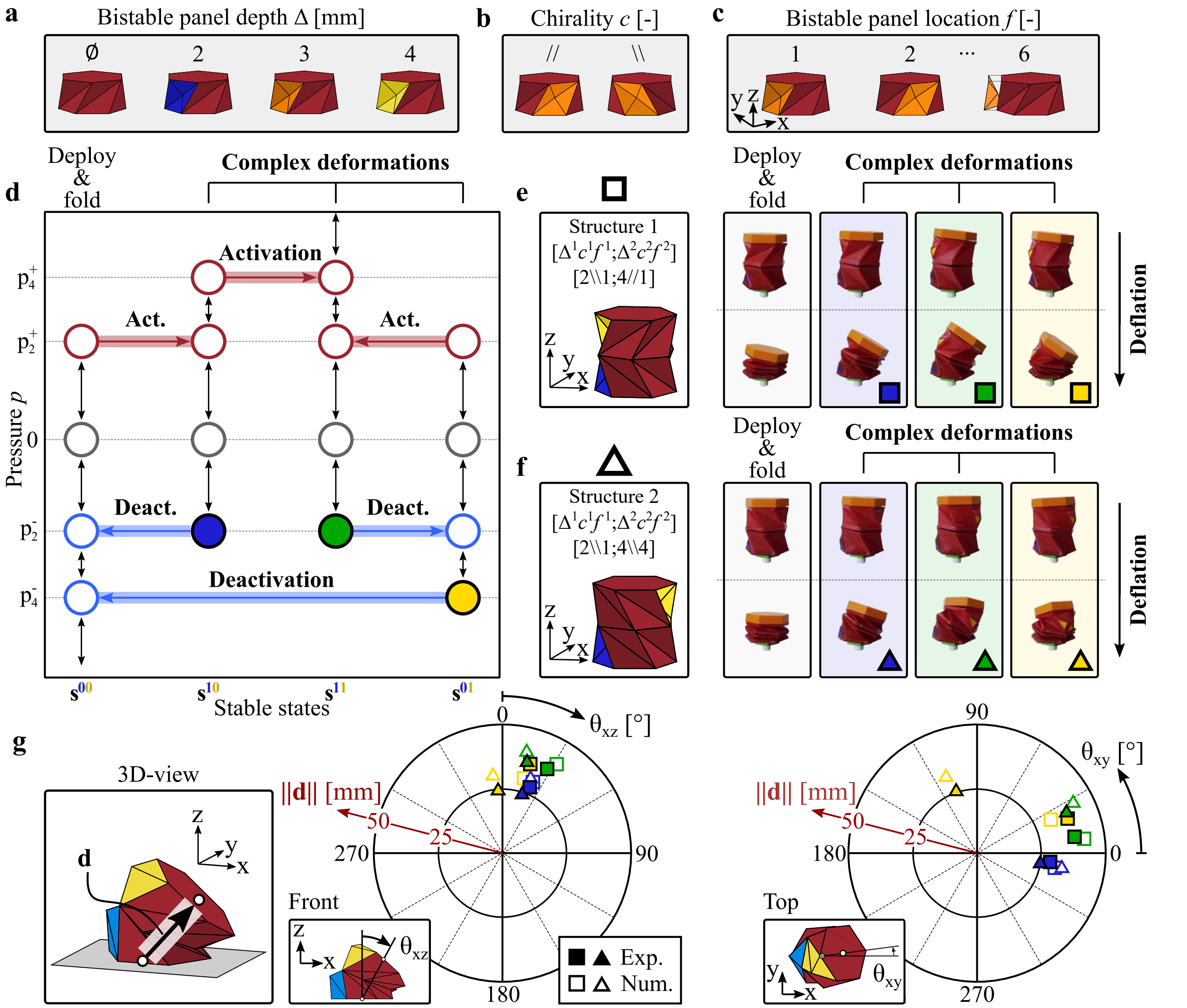

Fig. 2. Multimodal deformation via multistability. We create multi-unit structures by combining n modules. Each k^{th} module is defined by three geometrical parameters: **(a)** the modified panel depth, Δ^k, **(b)** the chirality of the Kresling pattern, c^k, and **(c)** the location of the modified panel, f^k. Note that, for simplicity, for the modified panel of the bottom unit we choose $f^1 = 1$, since it always faces the negative x-axis. **(d)** State diagram for any multi-unit structure with $\Delta \in \{2, 4\}$ mm. **(e)** Schematic of a 2-unit structure defined by $[\Delta^1 c^1 f^1; \Delta^2 c^2 f^2] = [2\backslash\backslash 1; 4//1]$ along with experimental snapshots of its different deformation modes under vacuum. **(f)** Schematic of a 2-unit structure defined by $[\Delta^1 c^1 f^1; \Delta^2 c^2 f^2] = [2\backslash\backslash 1; 4\backslash\backslash 4]$ along with experimental snapshots of its different deformation modes under vacuum. **(g)** Polar plots showing the angles in the xz-plane, θ_{xz}, and the xy-plane, θ_{xy}, associated to each state in the three different complex deformation modes for the two 2-unit structures. The radial distance of the markers represents the norm of the vector connecting the two caps' centroids, $||\mathbf{d}||$. Both experimental measurements (filled markers) and numerical predictions (empty markers) are shown.

once again track the vector connecting the bottom and top cap's centroids, $\mathbf{d}$, at the lowest pressure point of bending deformation associated to each state (see inset in Fig. 2g). We find that for the first structure the deformations associated to states s^{10}, s^{11}, and s^{01} are all bending-dominated and characterized by $\theta_{xz} \approx 20^\circ$ and $\theta_{xy} \in [-7.34^\circ, 20.4^\circ]$ (filled square markers in Fig. 2g). Differently, in the second structure, in addition to two off-axis bending modes with $\theta_{xz} \approx 20^\circ$ and $\theta_{xy} = -9.40$ and 23.9°, vacuum unlocks a distinct, twisting-dominated deformation mode characterized by $\theta_{xz} = -3.64^\circ$ and $\theta_{xy} = 108^\circ$ (filled triangular markers in Fig. 2g).

The results of Fig. 2 show that the arrangement of the modules within the tubular structure has a profound effect on the deformation modes associated with each stable state. To systematically explore such effect, we develop a simple algorithm that predicts the geometry of deformation under each mode. First, we extract key geometric features from the experiments conducted on single units, i.e. $||\mathbf{d}||$, θ_{xz} and θ_{xy} each deformation modes (see Figs. S4-S5). When assuming pressure continuity, these data allow the prediction of the geometry of deformation of any n-unit structure (see Supplementary Materials, Section S3 for details on the algorithm). Note that we also assume perfect coupling between units, so that the pressure thresholds, $p_\Delta^{+/-}$, found in the experimental

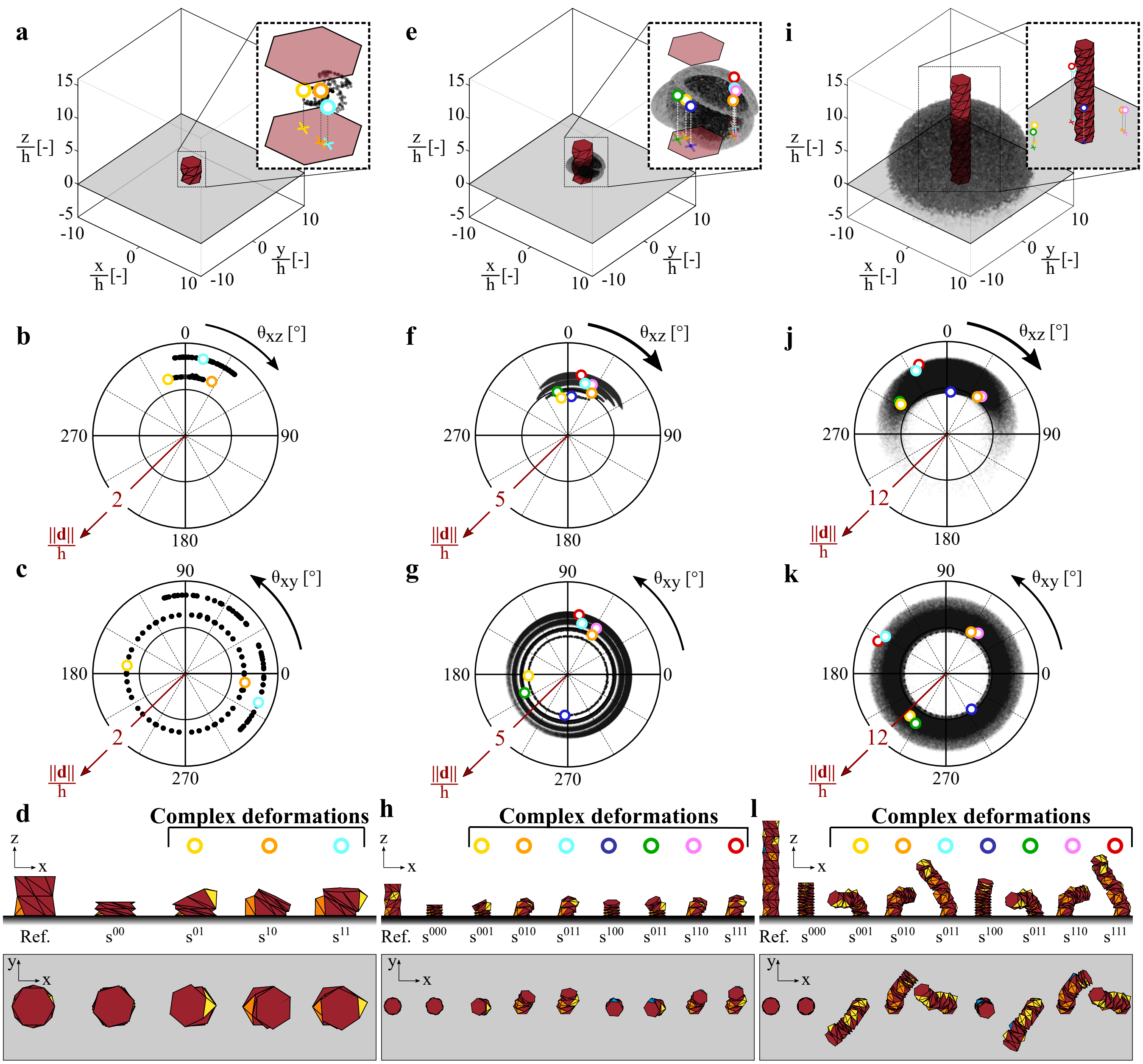

Fig. 3. Exploration of the design space. We use our numerical model to characterize the deformation modes of structures made of $n = 2, 4$, and 12 units. Location of the top cap's centroid (black dots) associated to each complex deformation modes of any structure made of $n = 2$ (**a**) and $n = 4$ (**e**) units as well as $500,000$ random structures with $n = 12$ (**i**) units. Note that we show $1,296$, $1.78e6$, and $4e6$ different top cap's locations (black dots) for $n = 2$, 4, and 12, respectively. Polar plots showing the angles in the xz-plane, θ_{xz}, and the xy-plane, θ_{xy}, associated to each state in the complex deformation modes for any structure made of 2 (**b-c**), 4 (**f-g**), and 12 (**j-k**) units. In all plots, the radial distance of the markers represents the norm of the vector connecting the two caps' centroids, $||\mathbf{d}||$. Numerical snapshots of the deformation modes of the structures with $n = 2$ (**d**), $n = 4$ (**h**), and $n = 12$ (**l**) units that maximizes Φ.

characterization of Fig. 1e, remain unchanged and identical for units with the same geometrical parameters. In Fig. 2g, we compare the results from our simple geometrical model (empty markers) with our experimental results (filled markers). Although experiments and model results are qualitatively similar, the error becomes large when the number of units in the structure increases. This error comes from the assumptions in the model, which does not take into account gravity, manufacturing imperfections as well as non-rigid coupling between the units (see Table S1 of the Supplementary Materials, Section 6 for the full quantification of the error between numerical predictions and experimental results).

Next, we use our numerical model to systematically investigate the deformation states that can be activated upon application of vacuum in our tubular structures. In Fig. 3a, we use black dots to show the location of the top cap's centroid at the lowest pressure for all complex deformation states (i.e. s^{ij} with $i + j > 0$) of any structure with $n = 2$ modules. For reference, we also depict the structure's bottom and top hexagonal plates under atmospheric pressure. When setting $f^1 = 1$, we find that most datapoints are clustered in a very narrow region that is contained within the top unit of the structure (see zoom-in in Fig. 3a). To further characterize the supported deformation states, we plot the angles θ_{xz} (Fig. 3b) and θ_{xy} (Fig. 3c) as a function of $||\mathbf{d}||/h$ for all datapoints. We find that the deformation modes for structures built out of only two modules are limited to the narrow range of $\theta_{xz} \in [-17.6°, 38.8°]$, whereas θ_{xy} spans the entire 360° range. Additionally, since our goal is to realize structures capable of switching between distinct deformation modes harnessing a single pressure source, we select the structure that maximizes

$$\Phi = \sum_{\alpha,\beta=1}^{n_{modes}} \frac{1}{2} \cdot ||\mathbf{d}_\alpha - \mathbf{d}_\beta||^2, \qquad [1]$$

where $n_{modes} = 2^{n_\Delta} - 1$ is the number of supported complex deformation modes (n_Δ denoting the number of different Δ used in the structure). We find that for $n = 2$ the most distinct deformation modes are achieved in a structure comprising two modules with the same chirality and modified panels located on opposite sides, i.e. $[\Delta^1 c^1 f^1; \Delta^2 c^2 f^2] = [3\backslash\backslash 1; 4\backslash\backslash 5]$. For this structure, states s^{10}, s^{01} and s^{11} are characterized by $\theta_{xz} = 25.9°$, $-17.2°$ and $13.1°$ and $\theta_{xy} = -8.51°$, $172°$ and $-21.5°$, respectively (see colored markers in Figs. 3a-c). As shown by the front and top views reported in Fig. 3d, the structure is able to bend in three different directions.

The complexity and number of deformation modes supported by the structures can be expanded by increasing the number of modules. In Figs. 3e-h and 3i-l, we report results for structures comprising $n = 4$ and $n = 12$ modules, respectively. Note that, since 38^n possible designs exist for a structure with n modules, while we can simulate all possible designs for $n = 4$, the number of designs for $n = 12$ is too large to perform an exhaustive search. Instead, we select $500,000$ random structure geometries. As expected, by increasing the number of modules in the structure, we extend the space attainable by the top cap's centroid (see Figs. 3e and 3i for $n = 4$ and 12, respectively). Specifically, in addition to θ_{xy} spanning the entire 360° range, we find that $||\mathbf{d}||/h \in [2.10, 3.40]$ and $[3.46, 10.1]$ and $\theta_{xz} \in [-44.5°, 63.3°]$ and full 360° range, respectively for $n = 4$ and 12 (see Figs. 3f-g and 3j-k) Finally, the numerical snapshots of the 4 and 12-unit structures that maximise Φ reported in Figs. 3h and 3l show that by controlling the input pressure these structures can be made to bend in a variety of directions as well as simply contract and twist under vacuum.

Inverse design to reach multiple targets

Building on the established platform, we now aim at demonstrating how one can design structures that can reach multiple targets in space, despite being actuated through a single pressure source. However, since the use of n modules leads to 38^n possible structure designs, it is crucial to use a robust algorithm to efficiently identify configurations leading to the targets. To this end, given the discrete nature of our design variables, we use a greedy algorithm based on the best-first search method (62, 63)—a progressive local search algorithm that, at each iteration, minimizes the cost function by looking at a set of available solutions. Although there exists many algorithms to solve this type of discrete optimization problems (64, 65), we find that the greedy algorithm provides the best trade-off between accuracy and computational cost (see Supplementary Materials, Section S4 for details and comparison of the different algorithms). Specifically, our greedy algorithm identifies tubular structures built out of n_s super-cells each with n_u modules (so that $n = n_u \cdot n_s$), whose tip can reach a desired set of targets arbitrarily positioned in the surrounding space. Note that the maximum number of targets a structure can reach is $n_{targets} = 2^{n_\Delta}$.At the first iteration, the algorithm starts by selecting the structure super-cell design that minimizes

$$\Psi = \frac{1}{n_{targets} \cdot h} \sum_{m=1}^{n_{targets}} \min ||\mathbf{d} - \mathbf{T}_m||, \qquad [2]$$

where $\mathbf{T}_m$ is the vector connecting the m-th target with the origin. Once the first super-cell is chosen, the algorithm stores it in memory and starts a second iteration. This comes to an end when the algorithm identifies a second super-cell that, connected to the first one, minimizes Eq. (2). The first two super-cells are then stored in memory and the algorithm advances to the next one. Note that in this study, to balance the number of available designs and computational cost, we set the greedy algorithm to consider super-cells made out of three units (i.e. $n_u = 3$, see Figs. S9 and S12 for a comparison across super-cells made with different n_u). Additionally, in order to avoid fabricating excessively long structures whose response could be affected by gravity, we impose that the algorithm should end after stacking five super-cells.

To demonstrate our approach, we select a set of targets within the reachable space (see red circular markers in Fig. 4a and Supplementary Materials Figs. S14-S15 for additional targets). In Fig. 4b we show the minimum value of the objective function Ψ identified by our algorithm at each iteration for the selected set of targets. Further, in Fig. 4c we report the deformed modes that most closely approach the three targets for the corresponding structures. We find that for this set of targets the minimum error is reached for a structure with $n_s = 4$ (note that the convex shape of Ψ in Fig. 4b is due to a correlation between the optimal number of units and the average distance of the targets from the origin—see Supplementary Materials Fig. S15). This design comprises the classic Kresling module as well as bistable units with $\Delta = 2$, 3, and 4 mm (see Fig. 4d). As such, the optimal structure has eight stable states, 14 snapping transitions, and a more complex state diagram in which not all targets are reached consecutively by continuously decreasing pressure (Fig. 4e). More specifically, to move from $T1$ to $T2$, this structure has to be reset by decreasing the pressure below p_3^- before increasing above p_4^+ and then lowering it to p_3^-. As such, in this case the centroid of the top plate of the structure passes through the straight configuration O when moving from $T1$ to $T2$ and its trajectory comprises two disconnected loops, $O - T1$ and $O - T2 - T3$ (Fig. 4f). Note that we can add additional constraints to our greedy algorithm to make sure the targets fall within the same closed loop on the state diagram. This leads to a different design and may increase the targets error, Ψ (see Supplementary Materials Fig. S13 for details). However, the ability to follow sequentially a discretized trajectory along a closed pressure loop makes the platform compelling for robotic applications (see Supplementary Materials, Section S5 for an example of a single-input robot capable of locomotion through multimodal deformation).

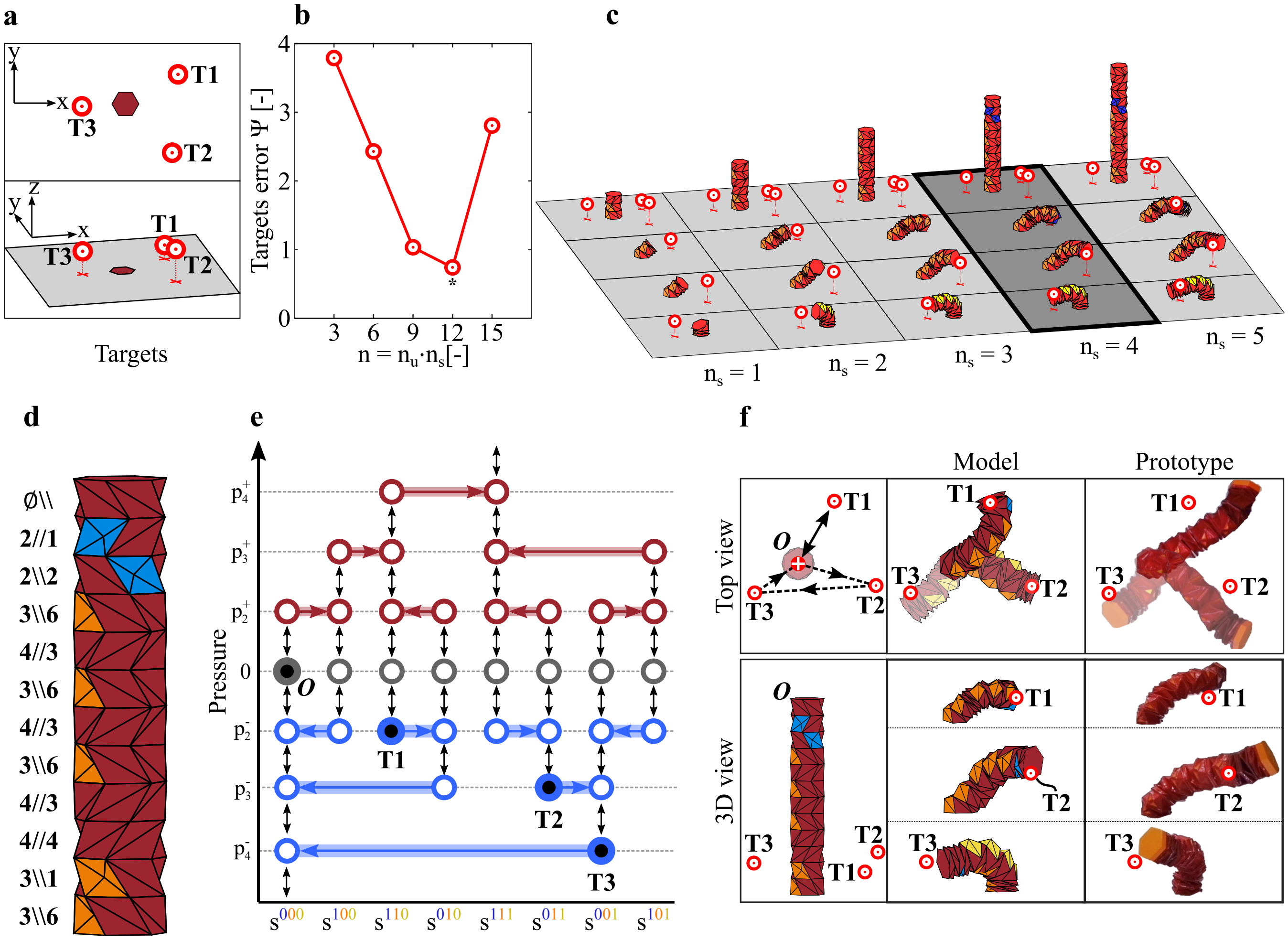

Fig. 4. Inverse design to reach multiple targets. We employ a greedy algorithm to inverse design structures able to reach a set of targets with a single pressure source. **(a)** Selected set of three targets (red dots), top and 3D view. **(b)**Targets error, Ψ, as a function of total number of units. **(c)** The three deformation modes that most closely match the three targets for the structures that minimize the target error Ψ. **(d)** The optimal structure produced by the algorithm along with the respective parameters for each module. **(e)** State diagram for the 12-unit, optimal structure $(*)$ with targets $T1$, $T2$ and $T3$ highlighted. **(f)** Top and 3D view of the model and the experimental prototype for the 12-unit optimal structure.

Conclusion

To summarize, in this work we have presented a platform to design tubular structures that can switch between distinct deformation modes using only one pressure input. The key component of our platform is an origami building block with a degree-four vertex panel, which can be geometrically programmed to snap at a certain input threshold, unlocking complex deformation modes upon vacuum. This, together with the position of the modified panel in the origami module and their direction of rotation, constitute the parameters of a rich design space that we can efficiently scan with a custom greedy algorithm. While in this study we have used a simple geometric model to identify optimal designs, a fully mechanical model (66, 67) that accounts for the effect of gravity, the pressure drop during the snap-through transition as well as the non-rigid coupling between the units would reduce the error between numerical predictions and experimental results. In addition, the current design space could be further expanded through investigating the effect of other geometrical parameters (e.g. l, h, and α) on the resulting deformation of the modules, as well as expanding the range of the considered values of Δ. While this could lead to more complex deformation modes and enhanced functionality, a drawback is a more complex state diagram. This means that a given structure might have to go through a longer loading history to reach some prescribed targets, increasing the operational time-span. A potential solution to this is to measure the volume at which the module snaps inward and outward, assume constant flow rate, and derive the time associated to each snapping transition. This time span could then be included as variable in the optimization algorithm, in order to find a design that reaches the target in the shortest possible time. Further, although in this study we have used a specific platform based on 3D-printed origami modules to realize multimodal deformation, the findings are not restricted to these specific structures and could be used in the design of other functional systems. However, we hereby only claim the successful implementation of our method by fabricating the modules with specific equipment, materials and geometrical parameters. If other equipment/materials/systems are employed, the reader should take care to verify that our findings are still valid. This is due to the fact that a chosen manufacturing technique might not be accurate enough to yield distinct input thresholds (i.e. internal pressures in our case) and to give rise to the distinct stable states. To conclude, given the recent advancement in origami fabrication across scales (25, 36, 68, 69), we envisage that our concept hereby presented could be employed in future applications where space is limited and simplified controls are required, such as space exploration, surgical devices, and rescue missions.

Materials and Methods

Details of the design, materials, and fabrication methods are summarized in Supplementary Materials, Section S1. The experimental procedure to measure the pressure-volume curve is described in Supplementary Materials, Section S2, along with additional experimental data. Details on the numerical model are provided in Supplementary Materials, Section S3. The optimization algorithms used in this study are described in detail in Supplementary Materials, Section S4. An example of a single-input robot capable of locomotion through multimodal deformation is reported in Supplementary Materials, Section S5. Finally, additional results are described in Supplementary Materials, Section S6.

Acknowledgments

We thank Eder Medina for his assistance in the development of the fabrication methodology. **Author contributions:** A.E.F., D.M., B.G. and K.B. proposed and developed the research idea. A.E.F designed and fabricated the samples. A.E.F., D.M., B.G. and L.K. performed the experiments. A.E.F. and D.M. designed the optimization. D.M. conducted the numerical calculations. A.E.F., D.M., and K.B. wrote the paper. K.B. supervised the research. **Funding:** Research was supported by the NSF grants DMR-2011754, DMR-1922321 and EFRI-1741685. **Competing interests:** The authors declare no conflict of interest. **Data and materials availability:** All data needed to evaluate the conclusions of this study are present in the paper or the Supplementary Materials.

Supplementary Materials

References

1. D. Rus and M. Tolley. Design, fabrication and control of soft robots. *Nature*, 521:467–475, 2015.
2. Benjamin Gorissen, Dominiek Reynaerts, Satoshi Konishi, Kazuhiro Yoshida, Joon-Wan Kim, and Michael De Volder. Elastic inflatable actuators for soft robotic applications. *Advanced Materials*, 29(43):1604977, 2017.
3. Carmel Majidi. Soft robotics: A perspective—current trends and prospects for the future. *Soft Robotics*, 1(1):5–11, 2014. . URL https://doi.org/10.1089/soro.2013.0001.
4. Ellen T. Roche, Robert Wohlfarth, Johannes T. B. Overvelde, Nikolay V. Vasilyev, Frank A. Pigula, David J. Mooney, Katia Bertoldi, and Conor J. Walsh. A bioinspired soft actuated material. *Advanced Materials*, 26(8):1200–1206, 2014. . URL https://onlinelibrary.wiley.com/doi/abs/10.1002/adma.201304018.
5. Elliot W. Hawkes, Laura H. Blumenschein, Joseph D. Greer, and Allison M. Okamura. A soft robot that navigates its environment through growth. *Science Robotics*, 2(8), 2017. . URL https://robotics.sciencemag.org/content/2/8/eaan3028.
6. Mark Runciman, Ara Darzi, and George P Mylonas. Soft robotics in minimally invasive surgery. *Soft robotics*, 2019.
7. Panagiotis Polygerinos, Zheng Wang, Kevin C Galloway, Robert J Wood, and Conor J Walsh. Soft robotic glove for combined assistance and at-home rehabilitation. *Robotics and Autonomous Systems*, 73:135–143, 2015.
8. Bobak Mosadegh, Panagiotis Polygerinos, Christoph Keplinger, Sophia Wennstedt, Robert F Shepherd, Unmukt Gupta, Jongmin Shim, Katia Bertoldi, Conor J Walsh, and George M Whitesides. Pneumatic networks for soft robotics that actuate rapidly. *Advanced functional materials*, 24(15):2163–2170, 2014.
9. Fionnuala Connolly, Conor J. Walsh, and Katia Bertoldi. Automatic design of fiber-reinforced soft actuators for trajectory matching. *Proceedings of the National Academy of Sciences*, 114 (1):51–56, 2017. ISSN 0027-8424. . URL https://www.pnas.org/content/114/1/51.
10. Ramses V. Martinez, Jamie L. Branch, Carina R. Fish, Lihua Jin, Robert F. Shepherd, Rui M. D. Nunes, Zhigang Suo, and George M. Whitesides. Robotic Tentacles with Three-Dimensional Mobility Based on Flexible Elastomers. *ADVANCED MATERIALS*, 25(2):205–212, JAN 11 2013. ISSN 0935-9648. .
11. Robert F. Shepherd, Filip Ilievski, Wonjae Choi, Stephen A. Morin, Adam A. Stokes, Aaron D. Mazzeo, Xin Chen, Michael Wang, and George M. Whitesides. Multigait soft robot. *Proceedings of the National Academy of Sciences of the United States of America*, 108(51): 20400–20403, 2011. ISSN 00278424. URL http://www.jstor.org/stable/23077257.
12. Benjamin Gorissen, Edoardo Milana, Arne Baeyens, Eva Broeders, Jeroen Christiaens, Klaas Collin, Dominiek Reynaerts, and Michael De Volder. Hardware sequencing of inflatable nonlinear actuators for autonomous soft robots. *Advanced Materials*, 31(3):1804598, 2019.
13. Nikolaos Vasios, Andrew J Gross, Scott Soifer, Johannes TB Overvelde, and Katia Bertoldi. Harnessing viscous flow to simplify the actuation of fluidic soft robots. *Soft robotics*, 2019.
14. Matthew A. Robertson and Jamie Paik. New soft robots really suck: Vacuum-powered systems empower diverse capabilities. *Science Robotics*, 2(9), 2017. . URL https://robotics.sciencemag.org/content/2/9/eaan6357.
15. Joran W. Booth, Dylan Shah, Jennifer C. Case, Edward L. White, Michelle C. Yuen, Olivier Cyr-Choiniere, and Rebecca Kramer-Bottiglio. Omniskins: Robotic skins that turn inanimate objects into multifunctional robots. *Science Robotics*, 3(22), 2018. . URL https://robotics.sciencemag.org/content/3/22/eaat1853.
16. Lindsey Hines, Kirstin Petersen, and Metin Sitti. Inflated soft actuators with reversible stable deformations. *Advanced Materials*, 28(19):3690–3696, 2016.
17. Eran Ben-Haim, Lior Salem, Yizhar Or, and Amir D Gat. Single-input control of multiple fluid-driven elastic actuators via interaction between bistability and viscosity. *Soft Robotics*, 7 (2):259–265, 2020.
18. Laura Paez, Gunjan Agarwal, and Jamie Paik. Design and analysis of a soft pneumatic actuator with origami shell reinforcement. *Soft Robotics*, 3(3):109–119, 2016. . URL https://doi.org/10.1089/soro.2016.0023.
19. Andrew D. Marchese, Cagdas D. Onal, and Daniela Rus. Autonomous soft robotic fish capable of escape maneuvers using fluidic elastomer actuators. *Soft Robotics*, 1(1):75–87, 2014. . URL https://doi.org/10.1089/soro.2013.0009. PMID: 27625912.
20. David Rostin Ellis, Martin Philip Venter, and Gerhard Venter. Soft pneumatic actuator with bimodal bending response using a single pressure source. *Soft Robotics*, 0(0):null, 0. . URL https://doi.org/10.1089/soro.2020.0017. PMID: 32846112.
21. Shuichi Wakimoto, Koichi Suzumori, and Keiko Ogura. Miniature pneumatic curling rubber actuator generating bidirectional motion with one air-supply tube. *Advanced Robotics*, 25 (9-10):1311–1330, 2011. . URL https://doi.org/10.1163/016918611X574731.
22. L. Zentner, V. Böhm, and V. Minchenya. On the new reversal effect in monolithic compliant

bending mechanisms with fluid driven actuators. *Mechanism and Machine Theory*, 44(5): 1009 – 1018, 2009. ISSN 0094-114X. . URL http://www.sciencedirect.com/science/article/pii/S0094114X08001134.

23. J.T.B. Rational design of reconfigurable prismatic architected materials. Overvelde, James C. Weaver, Chuck Hoberman, and Katia Bertoldi. Rational design of reconfigurable prismatic architected materials. *Nature*, 541:347–352, Jan 2017. . URL https://doi.org/10.1038/nature20824.
24. E. Hawkes, B. An, N. M. Benbernou, H. Tanaka, S. Kim, E. D. Demaine, D. Rus, and R. J. Wood. Programmable matter by folding. *Proceedings of the National Academy of Sciences*, 107(28): 12441–12445, 2010. ISSN 0027-8424. . URL https://www.pnas.org/content/107/28/12441.
25. David Melancon, Benjamin Gorissen, Carlos J. García-Mora, Chuck Hoberman, and Katia Bertoldi. Multistable inflatable origami structures at the metre scale. *Nature*, 592:545–550, 2021. .
26. Levi H. Dudte, Etienne Vouga, Tomohiro Tachi, and L. Mahadevan. Programming curvature using origami tessellations. *Nature Materials*, 15:583–588, Mar 2016. . URL https://doi.org/10.1038/nmat4540.
27. Erik D. Demaine and Tomohiro Tachi. Origamizer: A practical algorithm for folding any polyhedron. In *Proceedings of the 33rd International Symposium on Computational Geometry (SoCG 2017)*, pages 34:1–34:15, Brisbane, Australia, July 4–7 2017.
28. Zeang Zhao, Xiao Kuang, Jiangtao Wu, Qiang Zhang, Glaucio H. Paulino, H. Jerry Qi, and Daining Fang. 3d printing of complex origami assemblages for reconfigurable structures. *Soft Matter*, 14:8051–8059, 2018. . URL http://dx.doi.org/10.1039/C8SM01341A.
29. S. Felton, M. Tolley, E. Demaine, D. Rus, and R. Wood. A method for building self-folding machines. *Science*, 345(6197):644–646, 2014. ISSN 0036-8075. . URL https://science.sciencemag.org/content/345/6197/644.
30. Daniela Rus and Michael T. Tolley. Design, fabrication and control of origami robots. *Nature Reviews Materials*, 3(6):101–112, 2018. . URL https://doi.org/10.1038/s41578-018-0009-8.
31. Christian D. Santangelo. Extreme mechanics: Self-folding origami. *Annual Review of Condensed Matter Physics*, 8(1):165–183, 2017. . URL https://doi.org/10.1146/annurev-conmatphys-031016-025316.
32. Hiromi Yasuda, Yasuhiro Miyazawa, Efstathios G. Charalampidis, Christopher Chong, Panayotis G. Kevrekidis, and Jinkyu Yang. Origami-based impact mitigation via rarefaction solitary wave creation. *Science Advances*, 5(5), 2019. . URL https://advances.sciencemag.org/content/5/5/eaau2835.
33. H. Yasuda, C. Chong, E. G. Charalampidis, P. G. Kevrekidis, and J. Yang. Formation of rarefaction waves in origami-based metamaterials. *PHYSICAL REVIEW E*, 93(4), APR 15 2016. ISSN 2470-0045. .
34. M. Thota and K. W. Wang. Reconfigurable origami sonic barriers with tunable bandgaps for traffic noise mitigation. *JOURNAL OF APPLIED PHYSICS*, 122(15), OCT 21 2017. ISSN 0021-8979. .
35. M. Thota and K. W. Wang. Reconfigurable origami sonic barriers with tunable bandgaps for traffic noise mitigation. *JOURNAL OF APPLIED PHYSICS*, 122(15), OCT 21 2017. ISSN 0021-8979. .
36. Johannes T.B. Overvelde, Twan A. de Jong, Yanina Shevchenko, Sergio A. Becerra, George M. Whitesides, James C. Weaver, Chuck Hoberman, and Katia Bertoldi. A three-dimensional actuated origami-inspired transformable metamaterial with multiple degrees of freedom. *Nature Communications*, 7:10929, Mar 2016. . URL https://doi.org/10.1038/ncomms10929.
37. Arda Kotikian, Connor McMahan, Emily C. Davidson, Jalilah M. Muhammad, Robert D. Weeks, Chiara Daraio, and Jennifer A. Lewis. Untethered soft robotic matter with passive control of shape morphing and propulsion. *Science Robotics*, 4(33):eaax7044, 2019. .
38. Timothy G. Leong, Christina L. Randall, Bryan R. Benson, Noy Bassik, George M. Stern, and David H. Gracias. Tetherless thermobiochemically actuated microgrippers. *Proceedings of the National Academy of Sciences*, 106(3):703–708, 2009. ISSN 0027-8424. . URL https://www.pnas.org/content/106/3/703.
39. Ying Liu, Julie K. Boyles, Jan Genzer, and Michael D. Dickey. Self-folding of polymer sheets using local light absorption. *Soft Matter*, 8:1764–1769, 2012. . URL http://dx.doi.org/10.1039/C1SM06564E.
40. Qingkun Liu, Wei Wang, Michael F. Reynolds, Michael C. Cao, Marc Z. Miskin, Tomas A. Arias, David A. Muller, Paul L. McEuen, and Itai Cohen. Micrometer-sized electrically programmable shape-memory actuators for low-power microrobotics. *Science Robotics*, 6(52):eabe6663, 2021. .
41. Yoonho Kim, Hyunwoo Yuk, Ruike Zhao, Shawn A. Chester, and Xuanhe Zhao. Printing ferromagnetic domains for untethered fast-transforming soft materials. *Nature*, 558(33):274–279, 2018. .
42. Larissa S. Novelino, Qiji Ze, Shuai Wu, Glaucio H. Paulino, and Ruike Zhao. Untethered control of functional origami microrobots with distributed actuation. *Proceedings of the National Academy of Sciences*, 117(39):24096–24101, 2020. ISSN 0027-8424. . URL https://www.pnas.org/content/117/39/24096.
43. Shuai Wu, Qiji Ze, Jize Dai, Nupur Udipi, Glaucio H. Paulino, and Ruike Zhao. Stretchable origami robotic arm with omnidirectional bending and twisting. *Proceedings of the National Academy of Sciences*, 118(36), 2021. ISSN 0027-8424. . URL https://www.pnas.org/content/118/36/e2110023118.
44. Soroush Kamrava, Davood Mousanezhad, Hamid Ebrahimi, Ranajay Ghosh, and Ashkan Vaziri. Origami-based cellular metamaterial with auxetic, bistable, and self-locking properties. *Scientific Reports*, 7(1), 2017. . URL https://doi.org/10.1038/srep46046.
45. Brandon Hanna, Jason Lund, Robert Lang, Spencer Magleby, and Larry Howell. Waterbomb base: A symmetric single-vertex bistable origami mechanism. *Smart Materials and Structures*, 23:094009, 08 2014. .
46. Cai Jianguo, Deng Xiaowei, Zhou Ya, Feng Jian, and Tu Yongming. Bistable Behavior of the Cylindrical Origami Structure With Kresling Pattern. *Journal of Mechanical Design*, 137(6), 06 2015. ISSN 1050-0472. . URL https://doi.org/10.1115/1.4030158. 061406.
47. Jesse L. Silverberg, Jun-Hee Na, Arthur A. Evans, Bin Liu, Thomas C. Hull, Christian D. Santangelo, Robert J. Lang, Ryan C. Hayward, and Itai Cohen. Origami structures with a critical transition to bistability arising from hidden degrees of freedom. *Nature Materials*, 14: 389–393, 06 2015. ISSN 1050-0472. . URL https://doi.org/10.1038/nmat4232.
48. Scott Waitukaitis, Rémi Menaut, Bryan Gin-ge Chen, and Martin van Hecke. Origami multistability: From single vertices to metasheets. *Physical Review Letters*, 114(5), Feb 2015. ISSN 1079-7114. . URL http://dx.doi.org/10.1103/PhysRevLett.114.055503.
49. H. Yasuda and J. Yang. Reentrant origami-based metamaterials with negative poisson's ratio and bistability. *Phys. Rev. Lett.*, 114:185502, May 2015. . URL https://link.aps.org/doi/10.1103/PhysRevLett.114.185502.
50. Austin Reid, Frederic Lechenault, Sergio Rica, and Mokhtar Adda-Bedia. Geometry and design of origami bellows with tunable response. *Phys. Rev. E*, 95:013002, Jan 2017. . URL https://link.aps.org/doi/10.1103/PhysRevE.95.013002.
51. Ke Liu, Tomohiro Tachi, and Glaucio Paulino. Invariant and smooth limit of discrete geometry folded from bistable origami leading to multistable metasurfaces. *Nature Communications*, 10: 1–10, 09 2019. .
52. Benjamin Treml, Andrew Gillman, Philip Buskohl, and Richard Vaia. Origami mechanologic. *Proceedings of the National Academy of Sciences*, 115(27):6916–6921, 2018. ISSN 0027-8424. . URL https://www.pnas.org/content/115/27/6916.
53. Sahand Sadeghi and Suyi Li. Dynamic folding of origami by exploiting asymmetric multi-stability, 2020.
54. Jakob A. Faber, Andres F. Arrieta, and André R. Studart. Bioinspired spring origami. *Science*, 359(6382):1386–1391, 2018. ISSN 0036-8075. . URL https://science.sciencemag.org/content/359/6382/1386.
55. Stefano Mintchev, Jun Shintake, and Dario Floreano. Bioinspired dual-stiffness origami. *Science Robotics*, 3(20), 2018. . URL https://robotics.sciencemag.org/content/3/20/eaau0275.
56. B Kresling. Folded tubes as compared to Kikko ("Tortoise-Shell") bamboo. In Hull, T, editor, *ORIGAMI3*, pages 197–207, 2002. ISBN 1-56881-181-0. 3rd International Meeting of Origami Science, Mathematics, and Education, PACIFIC GROVE, CA, 2001.
57. Priyanka Bhovad, Joshua Kaufmann, and Suyi Li. Peristaltic locomotion without digital controllers: Exploiting multi-stability in origami to coordinate robotic motion. *Extreme Mechanics Letters*, 32:100552, 2019. ISSN 2352-4316. . URL http://www.sciencedirect.com/science/article/pii/S2352431619302202.
58. Alexander Pagano, Tongxi Yan, Brian Chien, A Wissa, and S Tawfick. A crawling robot driven by multi-stable origami. *Smart Materials and Structures*, 26(9):094007, aug 2017. . URL https://doi.org/10.1088/1361-665x/aa721e.
59. Joshua Kaufmann, Priyanka Bhovad, and Suyi Li. Harnessing the multistability of kresling origami for reconfigurable articulation in soft robotic arms. *Soft Robotics*, 0(0):null, 0. . URL https://doi.org/10.1089/soro.2020.0075. PMID: 33769099.
60. Hiromi Yasuda, Tomohiro Tachi, Mia Lee, and Jinkyu Yang. Origami-based tunable truss structures for non-volatile mechanical memory operation. *Nature Communications*, 8, 2017. . URL https://doi.org/10.1038/s41467-017-00670-w.
61. Hongbin Fang, Suyi Li, Huimin Ji, and K. W. Wang. Uncovering the deformation mechanisms of origami metamaterials by introducing generic degree-four vertices. *Phys. Rev. E*, 94:043002, Oct 2016. . URL https://link.aps.org/doi/10.1103/PhysRevE.94.043002.
62. S.A. Curtis. The classification of greedy algorithms. *Science of Computer Programming*, 49 (1):125–157, 2003. ISSN 0167-6423. . URL https://www.sciencedirect.com/science/article/pii/S0167642303000340.
63. Vincent Vidal. A lookahead strategy for heuristic search planning. pages 150–160, 01 2004.
64. Kusum Deep, Krishna Singh, M. Kansal, and Chander Mohan. A real coded genetic algorithm for solving integer and mixed integer optimization problems. *Applied Mathematics and Computation*, 212:505–518, 06 2009. .
65. Juliane Müller, Christine A. Shoemaker, and Robert Piché. So-i: a surrogate model algorithm for expensive nonlinear integer programming problems including global optimization applications. *Journal of Global Optimization*, 59(4):865–889, 2014. . URL https://doi.org/10.1007/s10898-013-0101-y.
66. K. Liu and G. H. Paulino. Nonlinear mechanics of non-rigid origami: an efficient computational approach[†]. *Proceedings of the Royal Society A: Mathematical, Physical and Engineering Sciences*, 473(2206):20170348, 2017. . URL https://royalsocietypublishing.org/doi/abs/10.1098/rspa.2017.0348.
67. Mojtaba Moshtaghzadeh, Ehsan Izadpanahi, and Pezhman Mardanpour. Prediction of fatigue life of a flexible foldable origami antenna with kresling pattern. *ENGINEERING STRUCTURES*, 251(A), JAN 15 2022. ISSN 0141-0296. .
68. Baris Bircan, Marc Z. Miskin, Robert J. Lang, Michael C. Cao, Kyle J. Dorsey, Muhammad G. Salim, Wei Wang, Paul L. Muller, David A. McEuen, and Itai Cohen. Bidirectional self-folding with atomic layer deposition nanofilms for microscale origami. *Nano Letters*, 20(7):4850–4856, 2020. . URL https://doi.org/10.1021/acs.nanolett.0c00824.
69. Qiji Ze, Shuai Wu, Jun Nishikawa, Jize Dai, Yue Sun, Sophie Leanza, Cole Zemelka, Larissa S. Novelino, Glaucio H. Paulino, and Ruike Renee Zhao. Soft robotic origami crawler. *Science Advances*, 8(13):eabm7834, 2022. . URL https://www.science.org/doi/abs/10.1126/sciadv.abm7834.